Published in final edited form as:
Bone. 2012 October ; 51(4): 810–818. doi:10.1016/j.bone.2012.07.021.

Mechanical loading, damping, and load-driven bone formation in mouse tibiae

Todd Dodge[a], **Mina Wanis**[a], **Ramez Ayoub**[b], **Liming Zhao**[a], **Nelson B. Watts**[c], **Amit Bhattacharya**[d], **Ozan Akkus**[e], **Alexander Robling**[a,f], and **Hiroki Yokota**[a,f,*]

[a]Department of Biomedical Engineering, Indiana University Purdue University Indianapolis, Indianapolis, IN 46202, USA

[b]Department of Biomedical Engineering, Purdue University, West Lafayette, IN 47907, USA

[c]Mercy Health Osteoporosis and Bone Health Services, Cincinnati, OH 45236, USA

[d]Department of Environmental Health, University of Cincinnati, Cincinnati, OH 45267, USA

[e]Department of Biomedical Engineering, Case Western Reserve University, Cleveland, OH 44106, USA

[f]Department of Anatomy and Cell Biology, Indiana University School of Medicine, Indianapolis, IN 46202, USA

Abstract

Mechanical loads play a pivotal role in the growth and maintenance of bone and joints. Although loading can activate anabolic genes and induce bone remodeling, damping is essential for preventing traumatic bone injury and fracture. In this study we investigated the damping capacity of bone, joint tissue, muscle, and skin using a mouse hindlimb model of enhanced loading in conjunction with finite element modeling to model bone curvature. Our hypothesis was that loads were primarily absorbed by the joints and muscle tissue, but that bone also contributed to damping through its compression and natural bending. To test this hypothesis, fresh mouse distal lower limb segments were cyclically loaded in axial compression in sequential bouts, with each subsequent bout having less surrounding tissue. A finite element model was generated to model effects of bone curvature *in silico*. Two damping-related parameters (phase shift angle and energy loss) were determined from the output of the loading experiments. Interestingly, the experimental results revealed that the knee joint contributed to the largest portion of the damping capacity of the limb, and bone itself accounted for approximately 38% of the total phase shift angle. Computational results showed that normal bone curvature enhanced the damping capacity of the bone by approximately 40%, and the damping effect grew at an accelerated pace as curvature was increased. Although structural curvature reduces critical loads for buckling in beam theory, evolution apparently favors maintaining curvature in the tibia. Histomorphometric analysis of the tibia revealed that in response to axial loading, bone formation was significantly enhanced in the regions that were predicted to receive a curvature-induced bending moment. These results suggest that in addition to bone's compressive damping capacity, surrounding tissues, as well as naturally-occurring bone curvature, also contribute to mechanical damping, which may ultimately affect bone remodeling and bone quality.

*Corresponding author at: Biomedical Engineering, Indiana University Purdue University Indianapolis, 723 West Michigan Street, SL220C, Indianapolis, IN 46202, USA. Fax: +1 317 278 5244. hyokota@iupui.edu (H. Yokota).

The authors report no conflicts of interest.

Keywords

Tibia loading; Ulna loading; Damping; Phase shift angle; Bone remodeling

Introduction

Osteoporotic fractures are a major public health concern. Recently, there has been a major effort to determine risk factors that might identify individuals who are at greater risk for incurring a fracture [1]. Those efforts have extended beyond the routine DXA-derived measures of bone mineral density and bone mineral content, and have been expanded to include so-called “bone quality” indices, which include measures of bone geometry and estimates of material properties. More recently, considerable interest has been generated in the “damping phenomenon” of the musculoskeletal system, particularly as it relates to bone fragility. Damping is the potential of the whole musculoskeletal system to effectively dissipate energy associated with loading. A recent set of clinical data indicates that postmenopausal women with vertebral fractures have low damping capacity at a number of different skeletal sites [2]. This intriguing observation suggests a potential, non-invasive diagnostic tool for evaluating susceptibility of bone fracture. However, because osteoporotic and fractured bone tends to present high damping [3,4], the mechanism underlying observed high damping in the healthy control group is unclear. The long-term objective of this study was to establish a functional linkage of the mechanical damping capacity of a body to a likelihood of bone fracture. In the current study, we sought to evaluate the individual contributions of bone and surrounding tissues, such as joints, skin, and muscle, to mechanical damping during loading.

In order to investigate the apparent discrepancy between damping capacity and fracture susceptibility, we addressed two questions: Is the contribution of joints, muscle, and skin larger than that of the underlying bone to mechanical damping? If the contribution of bone is significant, does its geometric configuration affect its damping capacity? We hypothesized that while joint and muscle tissue would provide the greatest contribution to the damping capacity, bone would have a significant effect and that increased bone curvature would enhance its damping capacity. To test the above hypotheses, we conducted a dynamical loading experiment (tibia loading) using mouse lower hindlimbs and determined two damping-related parameters: phase shift angle ($\Delta\theta$) and energy loss (ΔE) [5,6]. The phase shift angle was determined as a delay in a phase angle of displacement wave forms to a loading input, while energy loss was calculated as dissipative energy (hysteresis) per loading/unloading cycle. In order to examine the contribution of each of the tissues in the lower hindlimb, loading was applied using five different limb configurations (Samples I–V) in which the tissues such as skin, a foot, a knee, and muscle were sequentially removed and the structure was re-tested.

We also conducted numerical simulations using finite element (FE) models and evaluated the experimental data. A three-dimensional model reflecting the dimensions and curvature of a normal mouse tibia was constructed to test the effects of different geometries on the damping ability of the bone. Loads of 5 N at 0.5, 2, and 20 Hz were applied to this FE model for 10 s, and a phase shift angle was determined using the procedure identical for processing experimental data. To evaluate the effect of bone curvature on damping capacity, we determined the radius of curvature, d, and examined the tibia model with five different curvatures. While the tibia has a natural curvature in the medial–lateral and anterior–posterior directions, we focused on the medial–lateral direction of the curvature.

To examine a potential effect of bone curvature to load-driven bone formation, we conducted histomorphometric analysis using the tibia in response to axial loading. Because of the tibia's natural curvature, axial loading induces a bending moment that generates position-dependent stress. Using the tibia samples, we first predicted a curvature-dependent bone deformation throughout the length of the bone as well as the transverse sections at the proximal, middle, and distal regions. We then evaluated any linkage of fluorescently labeled newly formed bone surfaces to a predicted bending motion.

Materials and methods

Twenty-five mice (C57BL/6 male, ~16 weeks old) were used in this study. Experimental procedures were approved by the Indiana University Animal Care and Use Committee and were in compliance with the Guiding Principles in the Care and Use of Animals endorsed by the American Physiological Society.

Tibia loading for damping characterization

To evaluate mechanical damping in the lower limb, tibia loading was conducted to the right lower hindlimb of 18 mice with a voltage-regulated loading device (ElectroForce 3100, Bose, Inc.). The loading bout was 10 chains of a 5 N (peak-to-peak force) composite waveform consisting of a series of sinusoidal waves at varying frequencies. Each chain was composed of one cycle of the waves at 0.5 Hz and 1 through 20 Hz (1 Hz increments). These waves were connected at the highest peak, where the slope of each sinusoidal wave was equal to zero.

Loading was applied to five different sample configurations I–V (Fig. 1A). Those configurations were the intact lower hindlimb (Sample I), the limb without skin (Sample II), the limb without skin and foot (Sample III), the limb without skin, foot, and femur (Sample IV), and the tibia and fibula alone without an intact joint on either end, and having the surrounding soft tissues (*e.g.* musculature) removed (Sample V). Sample I was prepared from four additional anesthetized and euthanized animals, and the temporal change of phase shift angles after euthanasia was evaluated. Samples II–V were prepared only from the euthanized animals within 20 min after euthanasia.

Determination of a phase shift angle and energy loss

Phase shift angles between applied sinusoidal forces and displacements of the lower hindlimb were determined. Force (f) and displacement (L) were modeled as a sinusoidal wave:

$$f=A_f\sin(\omega t+\theta_f)+B_f \quad (1)$$

$$L=A_L\sin(\omega t+\theta_L)+B_L \quad (2)$$

and the phase shift angle was determined as $\Delta\theta = \theta_f - \theta_L$ using a least square-mean fit method with MatLab software (version 7.10, MathWorks). In response to a sinusoidal force waveform at 0.5 Hz, 2 Hz, and 20 Hz, energy loss, ΔE, was determined as a hysteresis loop integral.

Phase shift angle of the loading system

Prior to testing sample configurations I–V, we evaluated the phase shift angle that was induced by the loading device itself. Between the aluminum base and axial mover, we

placed a straight steel rod (20 mm long, and 3 mm in diameter). The phase shift angle of this configuration was treated as the contribution of the loading system.

Finite element (FE) model

MicroCT images of an isolated murine tibia were produced using a Scanco VivaCT 40 imaging machine (Scanco Medical AG). The images were reconstructed into a three-dimensional mesh using MIMICS 13.1 (Materialise, Inc.), in which the image was decomposed to approximately 10,000 tetrahedral units (Fig. 2A, left). The three-dimensional mesh was imported into COMSOL Multiphysics software (version 4.2, COMSOL Inc.), and dynamic loads of 5 N in a sinusoidal waveform at 0.5, 2, and 20 Hz were applied normal to the proximal end for 10 s. Material properties of cortical bone, such as Poisson's ratio, Young's modulus, and the damping ratio, were obtained from literature [7–9]. A phase shift angle was determined by using the same procedure as for analyzing experimental data.

A second three-dimensional finite element model of the tibia, built using the dimensions and radius of curvature derived from the microCT images obtained for the first model, was constructed using COMSOL Multiphysics software (Fig. 2A, right). Radius of curvature was defined as the maximum distance between the central axis of the bone and an imaginary axis spanning the center of the two ends of the bone. The same material properties used in the first FE model were also used in this model. To evaluate any effect of bone curvature on mechanical damping, the radius of curvature of the tibia model was altered between 0 and 150% the original value to determine the effect of curvature on mechanical damping in the tibia, creating a total of 5 new models (Fig. 2B). Dynamic loads of 5 N in a sinusoidal waveform at 0.5, 2, and 20 Hz were applied normal to each tibia model for 10 s, and a phase shift angle was determined using the procedure identical for analyzing experimental data.

Prediction of tibia bending

The three-dimensional mesh created from microCT images of the isolated tibia was imported into COMSOL Multiphysics software, and the bending mode was predicted using a built-in eigenfrequency solver. By "pinning" the bone at the ends, the boundary conditions were set to restrict the movement of tetrahedral units on the surface of the knee and ankle joints.

Tibia loading for histology

Three mice were used for tibia loading for histological analysis. The mouse was placed in an anesthetic induction-chamber to induce sedation and mask-anesthetized using 2% isoflurane. Using the ElectroForce loading device, axial loads of 5.0 N were applied at 2 Hz for 3 min per day for 3 consecutive days to the left tibia. The non-loaded right tibia was treated as a contralateral control. Mice were given an intraperitoneal injection of alizarin at 50 μg/g on day 5, and calcein at 30 μg/g on day 11. Animals were sacrificed 13 days after the last loading and the tibiae harvested for histological analysis. The isolated bones were cleaned of soft tissues and fixed with 10% neutral buffered formalin. They were embedded in methyl methacrylate, and the transverse sections were removed from the proximal (25%), middle (50%), and distal (75%) regions along the length of the tibia.

Statistical considerations

The mean and standard deviation of all data were calculated, and the Student's t test was used to determine statistical significance. P-values of less than 0.05 (*) were determined to be significant, with p-values of less than 0.01 (**) denoting a higher level of significance.

Results

The loading system was evaluated with anesthetized and euthanized animal models

The phase shift angle, induced by the loading device without any animal sample, was 1.1° at 0.5 Hz, 1.3° at 2 Hz, and 2° at 20 Hz. These angles were induced by the loader itself and removed from the contributions of bone and surrounding tissues. With animal samples, the phase shift angles for the sample configuration I gradually decreased after euthanasia (Fig. 1B). In response to the loading at 0.5 Hz, for instance, the ratio of measured phase shift angles in euthanized animals to anesthetized animals decreased from 0.99 immediately after euthanasia to 0.96, 0.89, and 0.81 after 20 min, 40 min, and 60 min, respectively, due to the natural post-mortem increase of stiffness. This time-dependent alteration of mechanical properties was found to lower the damping capacity of the intact hindlimb, potentially decreasing the observed phase shift angle of sample configurations I through IV in the following experiments. For this reason, in the experiments that required euthanized animals, we employed animals within 20 min after euthanasia to reduce the effects of post-mortem time-dependent alterations of mechanical response.

Determination of phase shift angles

In response to axial loading to the lower hindlimb, the representative force and displacement responses are depicted (Fig. 3). Loads were 5 N (peak-to-peak) in a series of individual sinusoidal components, including the frequencies 0.5 Hz and 1 through 20 Hz, at 1 Hz intervals. Loading at 0.5 Hz for sample configurations I and V generated displacements of 0.42 and 0.08 mm, respectively (Figs. 3A, C). At 2 Hz, sample configurations I and V produced displacements of 0.38 and 0.06 mm, respectively (Figs. 3B, D). Visible damage to the structure of the tibia resulting from the loading regimen was not observed in any of the samples.

A significant phase shift angle was observed for all sample configurations (Fig. 4). Note that the contribution of the loading system has been removed from the values shown. Among five configurations, phase shift angles of Samples I through III tended to increase slightly with increasing frequency, and no statistical difference was seen between these samples at any frequency ($p \geq 0.38$). Sample configuration I showed an increase in phase shift angle from 11.6° at 0.5 Hz to 13.7° at 20 Hz, and Samples II and III showed similar trends. Phase shift angles of Samples IV and V were significantly lower than those of Sample I at all frequencies, and showed very little dependence on frequency as frequency increased ($p < 0.001$). For example, sample configuration V produced a phase shift angle of 5.0° at 0.5 Hz and 3.9° at 20 Hz. The large drop in phase shift angle between Samples III and IV corresponded with the removal of the knee joint, and contributed to a 45%, 50%, and 68% decrease in phase shift angle at 0.5, 2, and 20 Hz, respectively. The ratio between the phase shift angle of stage V (bone alone) and stage I (intact hindlimb) demonstrated the influence of the tibia alone. This ratio was 43% at 0.5 Hz, 38% at 2 Hz, and 28% at 20 Hz. Removal of the ankle, skin, and muscle exhibited the smallest effects on phase shift angle, contributing to approximately 14% of the total phase shift at each frequency.

Determination of dissipation energy (energy loss)

In response to axial loading with a sinusoidal waveform at 0.5 Hz, the representative force–displacement relationships are illustrated (Figs. 5A–E). In those plots, the areas surrounded by closed loops correspond to dissipation energy due to hysteresis. Fig. 5F exhibits dissipation energy per cycle for the Samples I–V at 0.5, 2, and 20 Hz. At 0.5 Hz, dissipation energy gradually decreased between Samples I and III from 0.29 mJ to 0.25 mJ, respectively, with statistical significance seen between Samples I and III ($p < 0.03$). A much steeper, statistically significant drop was found between Samples I and IV in all frequency

groups ($p<0.001$). Samples IV and V showed very similar dissipation energies near 0.03 mJ per cycle. While similar trends in energy dissipation are seen in response to 2 and 20 Hz waveforms, the magnitude of the energy loss in each sample configuration decreased monotonously as the frequency was increased. The dissipation energy in Sample I was 0.29 mJ at 0.5 Hz, 0.27 mJ at 2 Hz, and 0.11 mJ at 20 Hz, and in Sample V decreased to 0.03 mJ at 0.5 and 2 Hz and 0.01 mJ at 20 Hz. The dissipation energy of the Sample V was approximately 9% that of Sample I at 0.5 and 2 Hz, and 11% at 20 Hz. Dissipation energy followed a similar trend as phase shift angle with a large decrease between Sample III and Sample IV. This drop, which corresponded with the removal of the knee joint, accounted for approximately 71%, 72% and 69% of the energy dissipated by the intact hindlimb at 0.5 Hz, 2 Hz, and 20 Hz, respectively. Skin was found to contribute to approximately 12% of the total dissipated energy at all frequencies, and the remaining energy was lost with removal of the muscle and foot.

Prediction by FE analysis

Phase shift angles in response to 0.5, 2, and 20 Hz sinusoidal waveforms were compared for each of the model derived from microCT images as well as for the models created to test the effects of curvature on damping. Using the microCT model, phase shift angles of 4.14°, 4.06°, and 4.09° were determined in response to force waveforms at 0.5, 2, and 20 Hz, respectively. Using the same material properties and radius of curvature, the curvature model predicted phase shift angles of 4.26°, 4.16°, and 4.41° at 0.5, 2, and 20 Hz, a difference of 2.8%, 2.4%, and 7.3%, respectively.

The radius of curvature was altered from the physiological value in a range of 0 to 1.66 mm, or 0 to 150% of the normal value to simulate the effects of curvature on phase shift angle (Fig. 6A). For d=0 mm (0% of normal), the phase shift angle was predicted to be 2.97° at 0.5 Hz, 3.02° at 2 Hz, and 3.04° at 20 Hz. These predicted phase shift angles were 44%, 38%, and 45% lower than those for a tibia with normal curvature at 0.5, 2, and 20 Hz, respectively. As the radius of curvature was changed to 0.83 mm (75% of normal), the predicted phase shift angle increased slightly to 3.56°, 3.51°, and 3.68° at 0.5, 2, and 20 Hz, respectively. As the radius of curvature further increased, the rate of increase of the phase shift angle was predicted to accelerate. At d=1.38 mm, or 125% of normal, the phase shift angle was predicted to be 4.99°, 5.07°, and 5.32° at 0.5, 2, and 20 Hz, respectively. Finally, at d= 1.66 mm (150% of normal), the predicted phase shift angle was 6.34° at 0.5 Hz, 6.30° at 2 Hz, and 6.39° at 20 Hz. In this highly-curved case, the predicted phase shift angles were 49%, 52%, and 45% higher than those for a normal tibia at 0.5, 2, and 20 Hz, respectively.

To evaluate the effects of certain material properties on the phase shift angle predicted by the model, sensitivity analysis simulations were conducted for the Young's modulus and damping ratio (Figs. 6B, C). Each variable was altered to between 50 and 150% of the value obtained from literature, while the radius of curvature and all other properties were held constant at their normal values. As Young's modulus increased, the FE model predicted that the phase shift angle would decrease at a decaying rate. As damping ratio increased, the model predicted that phase shift angle would increase linearly.

Bone histomorphometry

To evaluate a potential link between bone bending and load-driven bone formation, we examined the region of newly formed bone in response to tibia loading. FE analysis predicted that the primary tibia bending moved the proximal and middle parts in the mediolateral direction (Fig. 7A). The transverse sections corresponding to the sites at 25% and 50% along the length of the tibia from the proximal end significantly oscillates with the antero-posterior direction as neutral axis. Consistent with the positions of bending-moment

driven stress, tibia loading enhanced bone formation in the proximal and middle sections but no significant labeling was observed in the distal section (Fig. 7B). Furthermore, the medial and lateral surfaces were more strongly labeled than the anterior and posterior surfaces.

Discussion

The experimental data demonstrated that mouse lower hindlimbs exhibited substantial viscoelastic characteristic, and depending on the sample configurations and loading frequency dynamic loading induced 4–14° phase shift angles and 0.01–0.3 mJ energy loss per cycle. The maximum damping capacity was obtained for the intact lower hindlimb without any tissue removal. Interestingly, bone alone significantly contributed to the damping capacity, with approximately 43% of the total phase shift angle attributed to bone in response to loading at 0.5 Hz, declining as frequency increased to 28% at 20 Hz. Energy dissipated in the bone was found to be between 9 and 11% of that of the intact limb at all frequencies.

Most of the remaining portion of the damping capacity of the lower hindlimb was a result of the knee joint and muscle tissue surrounding the bone, with the skin and ankle joint adding very little influence. The small contribution of the ankle joint might be a result of the boundary conditions of the experimental setup, as both the ankle in sample configuration II and the distal end of the tibia in sample configuration III were potted in the base of the loader. The knee joint alone accounted for approximately 45–58% of the total phase shift angle, and approximately 69–72% of the dissipated energy, depending on frequency. This result suggests that the knee joint, in addition to bone, plays a significant role in the damping capacity of the hindlimb.

Given that the removal of the femur corresponds to the greatest structural change to the system, the presence or absence of the femur seems important in load distribution and damping capacity. The distal mouse femur is composed primarily of spongy trabecular bone and has a thin cortex. The knee joint itself also contains tissues that contribute to damping in the limb, such as the meniscus, that were removed with the femur. This removal altered the stiffness of the remaining sample, and the boundary condition at the interface of the sample and the loader was also changed. Since derivation of phase shift angle and dissipation energy is affected by the changes in the stiffness and the boundary condition, the observed alteration in phase shift angle and dissipation energy was not solely induced by damping capacity of the removed tissue.

In a simple phase shift model such as a Voigt model, a quasi-proportional relationship is predicted between a phase shift angle and energy loss. However, in our experiments, phase shift angle and dissipation energy produced varied estimations of the contribution of bone to the damping capacity of the lower limb. The most likely cause of these differences involves nonlinear viscoelastic properties of bone [10,11]. These properties became evident when loading was applied to the bone. The displacement of bone was shown to exhibit an asymmetrical pattern in response to a sinusoidal load. As a compressive force was applied to the bone, the phase shift angle between the load and displacement was very small. However, during decompression, the phase shift angle increased as the recovery of the bone lagged behind the removal of force. Due to the varying phase shift, the least mean-square method used in data fitting may have overestimated the phase shift angle between the force and displacement in all sample configurations.

Hysteresis curves were also affected by the asymmetrical phenomenon. Unlike the compression portion of the hysteresis curve, the part of the curve corresponding to decompression to the preloaded state does not follow a path consistent with what is expected

from simple viscoelastic models. Instead, non-linear viscoelastic properties cause the decompression curve to mirror the compression curve, forming a crescent-shaped hysteresis loop. This phenomenon leads to a lower energy loss than might be expected in all sample configurations.

FE analysis predicted that curvature has a significant impact on the damping capacity of the tibia. Phase shift angles produced in a normal tibia model (d=1.1 mm) were predicted to be 4.26° at 0.5 Hz, 4.16° at 2 Hz, and 4.41° at 20 Hz. When the radius of the curvature was reduced to zero, simulating a straight bone, the phase shift angle decreased to approximately 3° at all frequencies. This result suggests that bending due to natural curvature accounts for approximately 38–45% of the total damping capacity of a normal tibia depending on frequency, with the remaining portion due to internal compressive properties. As the radius of curvature of the tibia model was increased to 1.66 mm, simulating a highly-curved bone, phase shift angles were predicted to increase by approximately 45–52% (depending on frequency) when compared to a tibia of natural curvature, or approximately 110% when compared to a zero-curvature model. This result indicates that increased curvature non-linearly enhances mechanical damping in the tibia.

Histomorphometric analysis supports the notion that bone curvature enhances load-driven bone formation on the periosteal surface in a position dependent manner. In tibia loading, FE analysis predicted the first vibration mode depicted in Fig. 7A. This mode with the resonance frequency at ~10 Hz is mainly caused by bone curvature in the proximal half of the tibia and it significantly deforms the proximal and middle portions without deforming the distal portion. The bending motion is predicted along the mediolateral direction, which is consistent with enhanced fluorescent signals on the medial and lateral surfaces of the proximal and middle transverse sections. The frequency for tibia loading in this study was 2 Hz, and the first vibration mode was lowest and closest to the loading frequency. Other vibration modes at higher frequencies present different bending patterns and the FE and histological results suggest that bone curvature is involved in its load-driven bone formation in a frequency and position dependent fashion. Collectively, bone curvature contributes to not only mechanical damping in bone but also load-driven bone formation.

Evolution of the geometric shape of bones is thought to be determined by a variety of environmental factors. For example, the shape of the human femur is thought to be impacted by climate adaptation [12]. Therefore, it is conceivable that temperature may also be a factor in the shape of the tibia. Other studies have proposed that bone shape is affected by loading during activity. For example, it has been suggested that the consistency of bending-induced strain patterns developed in long bones during physical activity may explain why curvature is a desirable structural aspect [13]. Furthermore, it has been proposed that the curved shape of long bones, while reducing overall axial strength, increases predictability and better distributes stresses within the bone during loading [14]. Curvature has also been identified as an important modulator of bone stiffness during development [15]. Of the bone configurations considered in this study, the greatest axial strength corresponded to a perfectly columnar tibia with no curvature (d=0 mm). This configuration, however, was found to significantly decrease the damping capacity of the bone and reduces bending motion. The configuration corresponding to the largest damping capacity and bending motion was a highly-curved shape (d=1.66 mm); however, this shape reduced axial strength. Collectively, the results of this study suggest that the appropriate amount of bone curvature may enhance shock-absorbing dampening effects and stimulate bone remodeling, but excessive curvature may induce detrimental effects.

Similar experiments have been performed using axial tibia loading on mice at frequencies 20 to 150 Hz [16]. The current experiments differ from this work, since we used a frequency

range of 0.5 to 20 Hz. This lower frequency range is consistent with previously performed mouse loading studies, in addition to results from clinical data that demonstrated importance of the phase shift angle in this range [2].

The current study has limitations in the experimental setup and computational simulations. First, we employed the loading conditions with 5 N (peak-to-peak) force in a sinusoidal wave, and loading was applied to euthanized animals. Differences in a phase shift angle between the anesthetized and euthanized animals were approximately 4% when the experiment was conducted within 20 min after euthanasia. Damping of bone and surrounding tissues is dependent on the loading and tissue conditions, and data in this study needs to be interpreted under these experimental conditions. Second, the FE analysis focused only on the tibia, excluding effects of the surrounding soft tissues and the fibula. A more comprehensive three-dimensional model could be developed to investigate damping in all surrounding soft tissues. Third, intramedullary fluid in a bone cavity is reported to move in response to mechanical loading and thus its effect on damping should be evaluated [17,18].

In this study we demonstrate that a skeleton including bone and surrounding tissues exhibit a significant capacity of mechanical damping. All tissues including bone, skin, cartilage, and muscle contribute to damping capacity through phase shift and energy loss. The fracture resistance of a bone has been suggested to be reliant on the bone's capacity to mechanically damp loads [19]. To achieve low incidence of bone fracture, bone curvature has been considered to be a negative factor because it reduces structural strength by lowering critical loads for buckling [20]. However, this study presents a novel finding that a small amount of bone curvature is beneficial for mechanical damping and curvature of the tibia is an outcome of a process of natural selection. In addition, it contributes to enhancing load-driven bone formation in a position dependent manner. The link between bone curvature and fracture susceptibility has been studied [21], in which the relationship between sagittal spinal curvature and the incidence of vertebral fractures was evaluated. It is concluded that reduction of the curvature led to increased fracture risk by more than eightfold, and their results are consistent with our analysis in the tibia. The further evaluation of mechanical damping during impact loading might help determine risk factors that can be clinically used to identify individuals who are at greater risk for incurring a fracture.

Acknowledgments

We thank Shana Ellis and Muller Soliman for technical support. This study was supported by the National Institute for Occupational Safety and Health Pilot Research Project Training Program of the University of Cincinnati Education and Research Center Grant T42/OH008432-06 and NIH R01AR052144.

References

1. Schuit SCE, van der Klift M, Weel AEAM, de Laet CEDH, Burger H, Seeman E, et al. Fracture incidence and association with bone mineral density in elderly men and women: the Rotterdam Study. Bone. 2004; 34:195–202. [PubMed: 14751578]
2. Bhattacharya A, Watts NB, Davis K, Kotowski S, Shukla R, Dwivedi AK, et al. Dynamic bone quality: a noninvasive measure of bone's biomechanical property in osteoporosis. J Clin Densitom. 2010; 13:228–36. [PubMed: 20347363]
3. Panteliou SD, Xirafaki AL, Panagiotopoulos E, Varakis JN, Cagenas NV, Kontoyannis CG. Modal damping for monitoring bone integrity and osteoporosis. J Biomech Eng. 2004; 12:1–5. [PubMed: 15171123]
4. Yeni YN, Shaffer RR, Baker KC, Dong XN, Grimm MJ, Les CM, et al. The effect of yield damage on the viscoelastic properties of cortical bone tissue as measured by dynamic mechanical analysis. J Biomed Mater Res. 2007; 82A:530–7.

5. Linde F, Hvid I, Pongsoipetch B. Energy absorptive properties of human trabecular bone specimens during axial compression. J Orthop Res. 1989; 7(3):432–9. [PubMed: 2703935]
6. Yamashita J, Furman BR, Rawis HR, Wang X, Agrawal CM. The use of dynamic mechanical analysis to assess the viscoelastic properties of human cortical bone. J Biomed Mater Res. 2001; 58(1):47–53. [PubMed: 11152997]
7. Roderic, L. Viscoelastic solids. Blackwell Publisher; 1998.
8. Chattah N, Sharir A, Weiner S, Shahar R. Determining the elastic modulus of mouse cortical bone using electronic speckle pattern interferometry (ESPI) and micro computed tomography: a new approach for characterizing small-bone material properties. Bone. 2009; 45(1):84–90. [PubMed: 19332167]
9. Fortis AP, Kostopoulos V, Panagiotopoulos E, Tsantzalis S, Kokkinos A. Viscoelastic properties of cartilage–subchondral bone complex in osteoarthritis. J Med Eng Technol. 2004; 28:223–6. [PubMed: 15371002]
10. Yamashita J, Li X, Furman BR, Rawls HR, Wang X, Agrawal CM. Collagen and bone viscoelasticity: a dynamic mechanical analysis. J Biomed Mater Res. 2002; 63:31–6. [PubMed: 11787026]
11. Fondrk M, Bahniuk E, Davy DT, Michaels C. Some viscoplastic characteristics of bovine and human cortical bone. J Biomech. 1988; 21:623–30. [PubMed: 3170617]
12. Weaver TD. The shape of the Neandertal femur is primarily the consequence of a hyperpolar body form. Proc Natl Acad Sci U S A. 2003; 100(12):6926–9. [PubMed: 12761384]
13. Biewener AA. Musculoskeletal design in relation to body size. J Biomech. 1991; 24(Suppl 1):19–29. [PubMed: 1791177]
14. Bertram JE, Biewener AA. Bone curvature: sacrificing strength for load predictability? J Theor Biol. 1988; 131:75–92. [PubMed: 3419194]
15. Main RP, Lynch ME, van der Meulen MC. *In vivo* tibial stiffness is maintained by whole bone morphology and cross-sectional geometry in growing female mice. J Biomech. 2010; 43:2689–94. [PubMed: 20673665]
16. Christiansen BA, Bayly PV, Silva MJ. Constrained tibial vibration in mice: a method for studying the effects of vibrational loading of bone. J Biomech Eng. 2008; 130(4):044502. [PubMed: 18601464]
17. Ozcivici E, Luu YK, Rubin CT, Judex S. Low-level vibrations retain bone marrow's osteogenic potential and augment recovery of trabecular bone during reambulation. PLoS One. 2010; 5:e11178. [PubMed: 20567514]
18. David V, Martin A, Lagage-Proust MH, Malaval L, Peyroche S, Jones DB, et al. Mechanical loading down-regulates peroxisome proliferator-activated receptor g in bone marrow stromal cells and favors osteoblastogenesis at the expense of adipogenesis. Endocrinology. 2007; 148:2553–62. [PubMed: 17317771]
19. Burr DB. Why bones bend but don't break. J Musculoskelet Neuronal Interact. 2011; 11(4):270–85. [PubMed: 22130136]
20. Milgrom C, Giladi M, Simkin A, Rand N, Dedem R, Kashtan H, et al. The area moment of inertia of the tibia: a risk factor for stress fractures. J Biomech. 1989; 22:1243–8. [PubMed: 2625424]
21. Kobayashi T, Takeda N, Atsuta Y, Matsuno T. Flattening of sagittal spinal curvature as a predictor of vertebral fracture. Osteoporos Int. 2008; 19(1):65–9. [PubMed: 17874033]

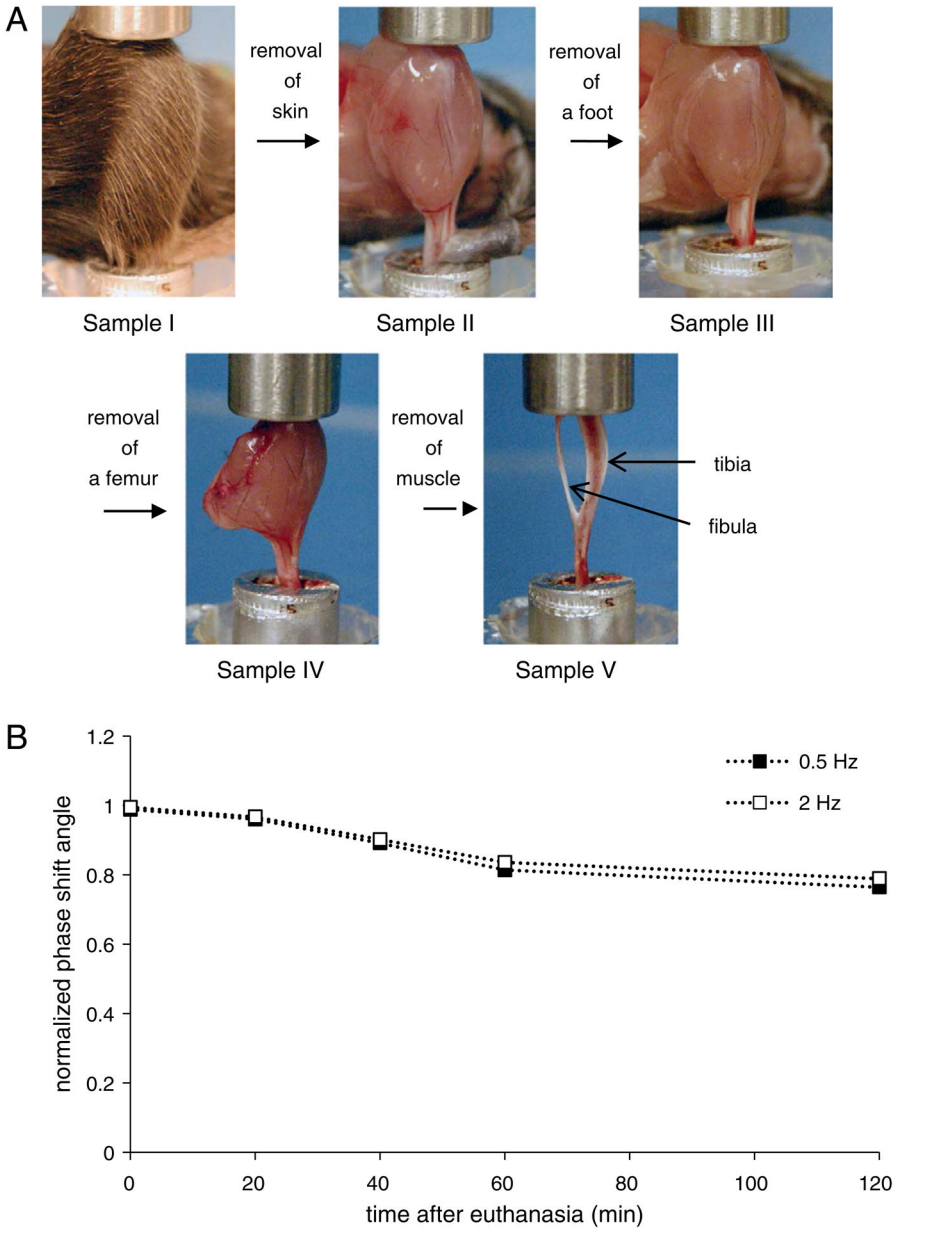

Fig. 1.

Sample configurations for analyzing damping using tibia loading and the effects of euthanasia. (A) Experimental sample configurations I–V for tibia loading: I—intact lower hindlimb; II—limb without skin; III—limb without skin and foot; IV—limb without skin, foot, and femur; and V—limb without skin, foot, femur, and muscle. (B) Phase shift angles of the sample configuration I as a function of time after euthanasia, normalized using the phase shift angle obtained from the anesthetized animal. The loading frequencies are 0.5 Hz and 2 Hz.

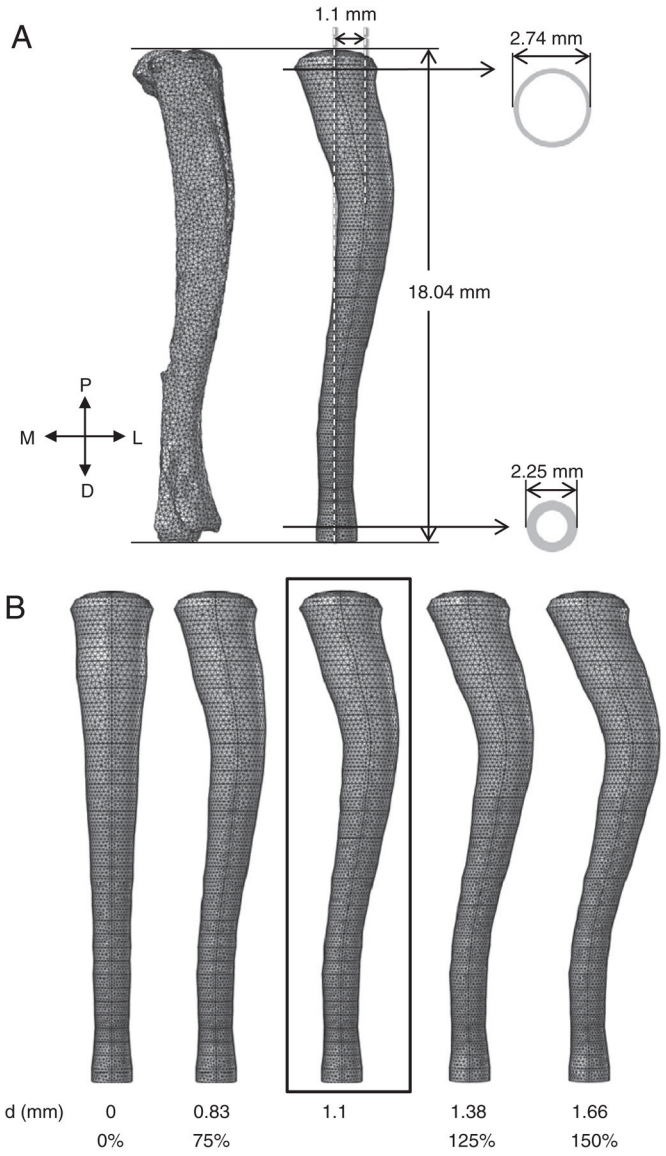

Fig. 2.

FE model configuration. (A) A model derived from microCT scans of a tibia (left) was used to create a FE model with the same dimensions and radius of curvature as the original tibia. Cross sections from the proximal and distal parts of the model demonstrate the interior structure of the cortical bone. The letter labels are: M—medial; L—lateral; P—proximal; and D—distal. (B) Additional FE models of the tibia were created by changing the radius of curvature of the original FE model of the tibia (boxed) to values 25% and 100% lower, along with 25% and 50% higher.

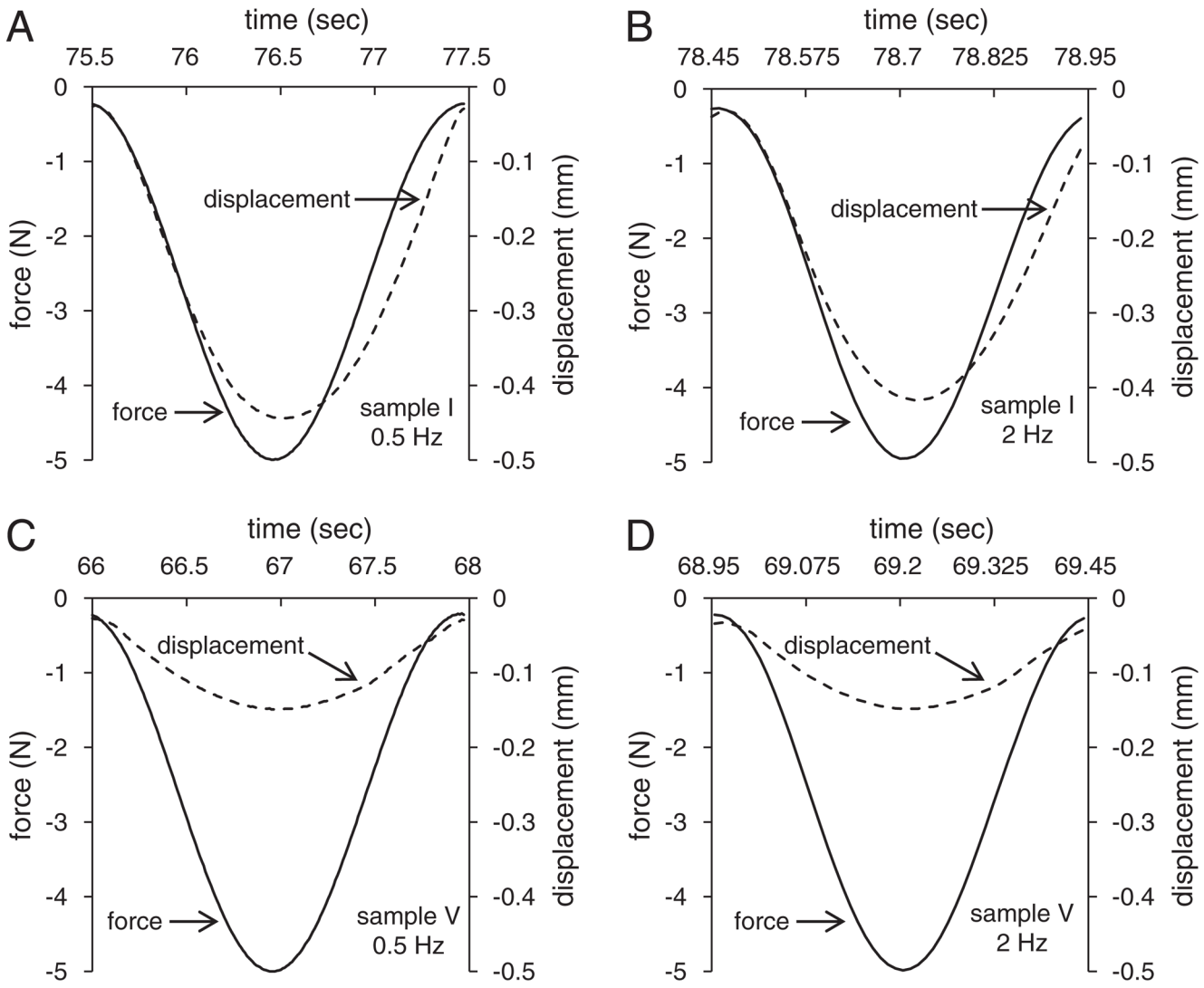

Fig. 3.

Force and displacement diagram. (A) Loading at 0.5 Hz for the sample configuration I. (B) Loading at 2 Hz for the sample configuration I. (C) Loading at 0.5 Hz for the sample configuration V. (D) Loading at 2 Hz for the sample configuration V.

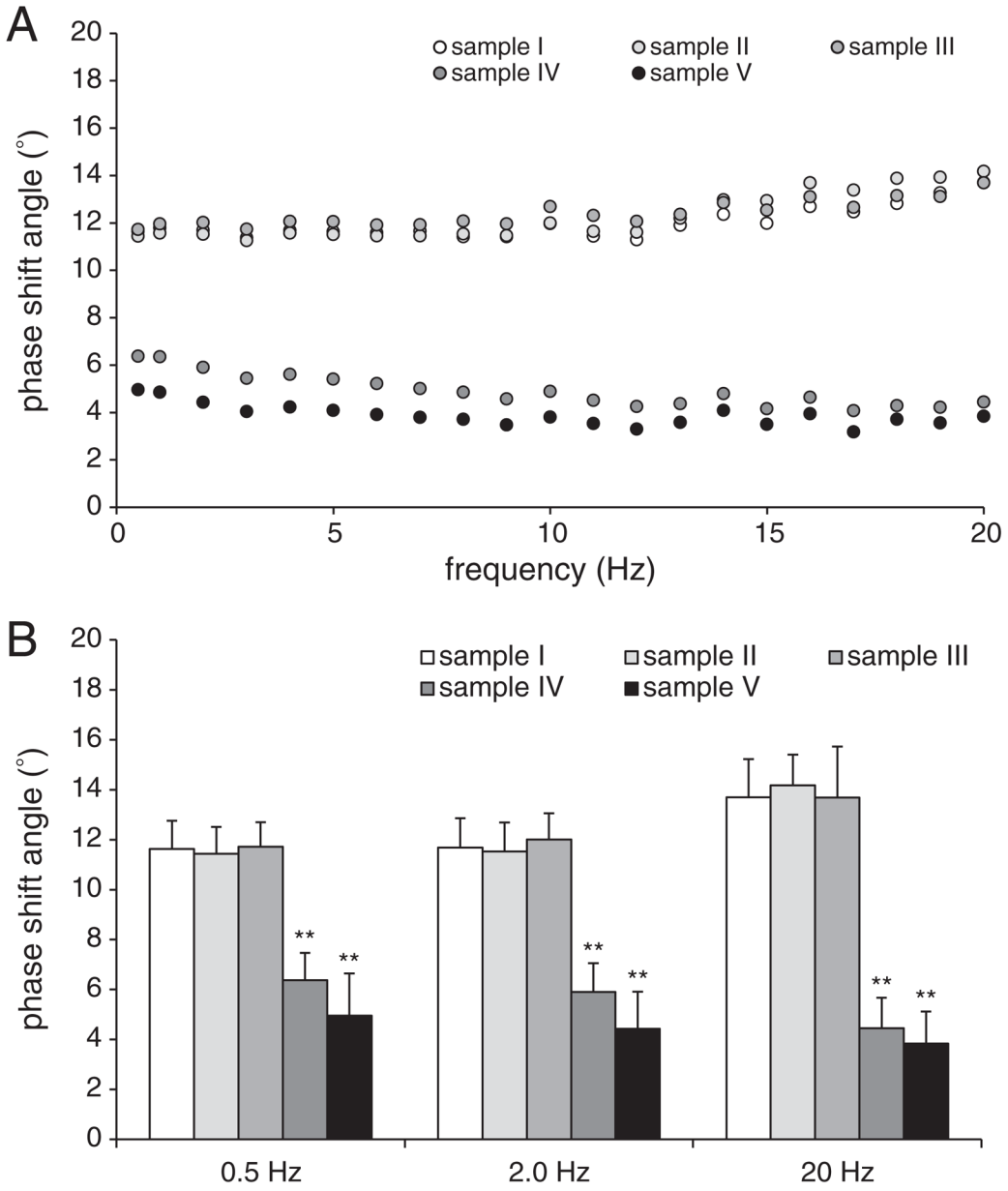

Fig. 4.

Effects of loading frequency on phase shift angle. (A) Phase shift angles for the sample configurations I–V in response to a force waveform consisting of a series of individual sinusoidal components from 0.5 to 20 Hz. (B) Phase shift angles for sample configurations I–V at 0.5, 2, and 20 Hz. Significance denoted in reference to sample configuration I.

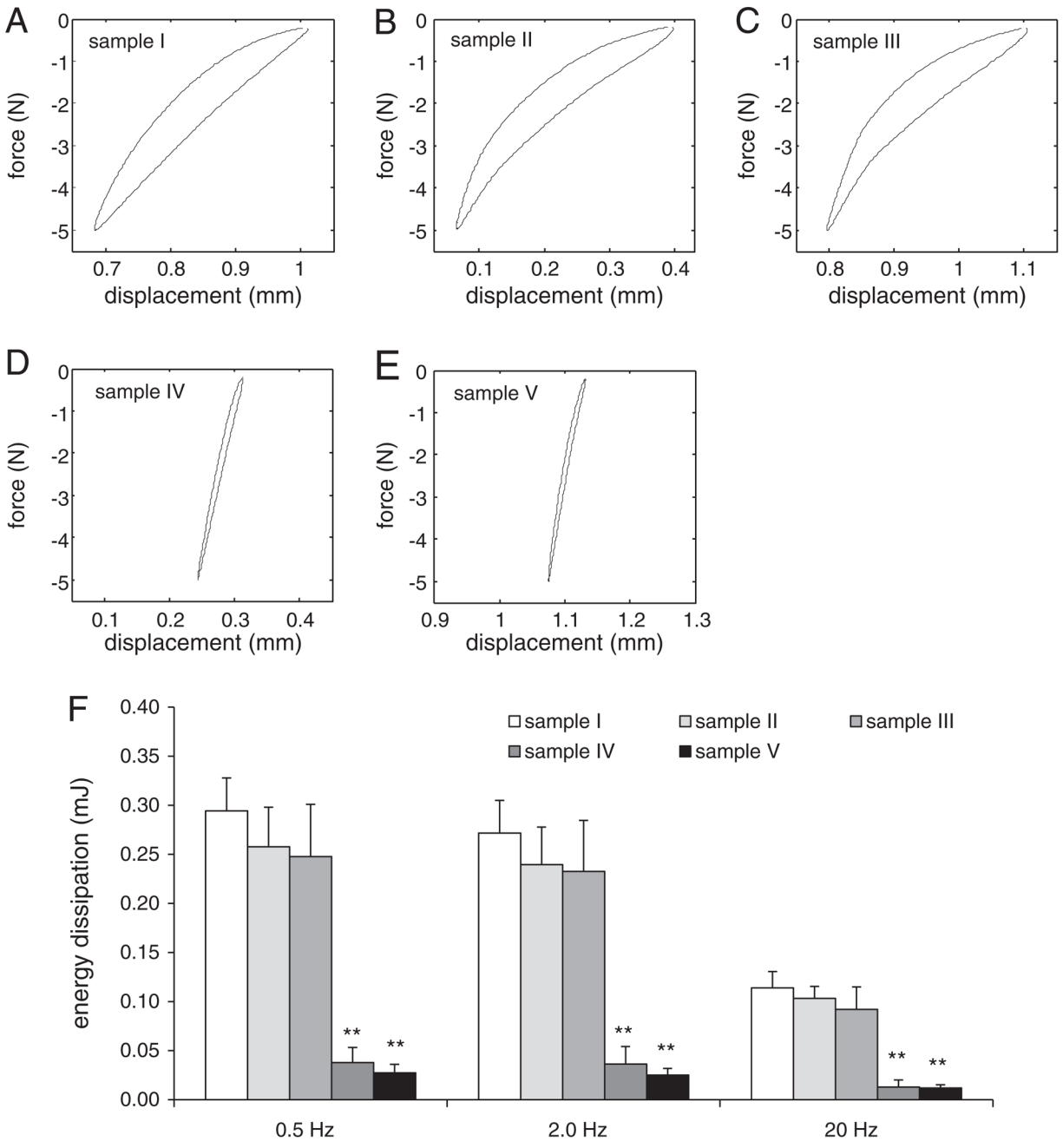

Fig. 5.

Force–displacement relationship and energy loss. (A) Loading at 0.5 Hz for the sample configuration I. (B) Loading at 0.5 Hz for the sample configuration II. (C) Loading at 0.5 Hz for the sample configuration III. (D) Loading at 0.5 Hz for the sample configuration IV. (E) Loading at 0.5 Hz for the sample configuration V. (F) Energy loss for the sample configurations I–V in response to loading at 0.5, 2, and 20 Hz. Significance denoted in reference to sample configuration I.

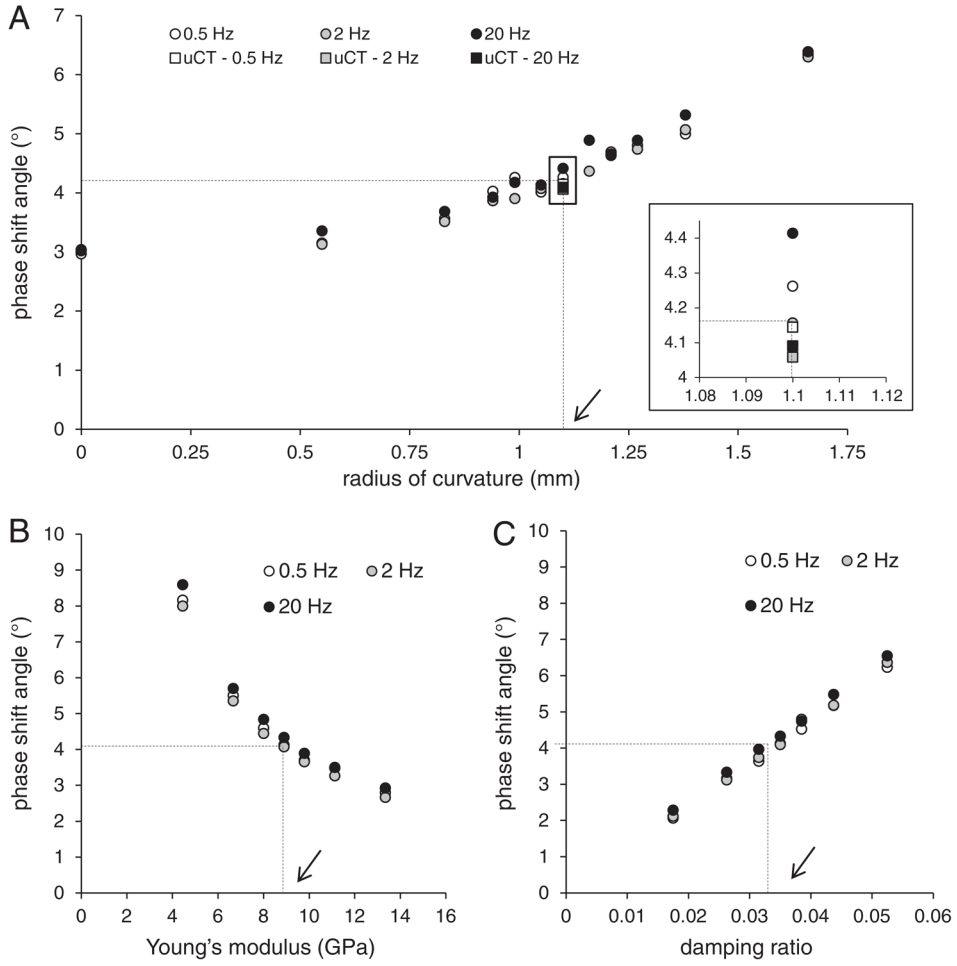

Fig. 6.

FE prediction of phase shift angle. FE models were subjected to sinusoidal force waveforms at 0.5, 2, and 20 Hz. (A) Prediction of the phase shift angles as a function of the maximum radius of curvature of the tibia. The dotted lines pinpoint the location of the physiologically normal model, with the arrow corresponding to 1.1 mm. Inset rectangle shows a zoomed view of the area surrounded by a box. (B) Sensitivity analysis showing the predicted phase shift angles when the elastic modulus of the model is altered. The dotted lines demonstrate the location of the physiologically normal model, with the arrow corresponding to 8.9 GPa. (C) Sensitivity analysis showing the predicted phase shift angles when the damping ratio of the model is altered. The dotted lines show the location of the physiologically normal model, with the arrow corresponding to 0.035.

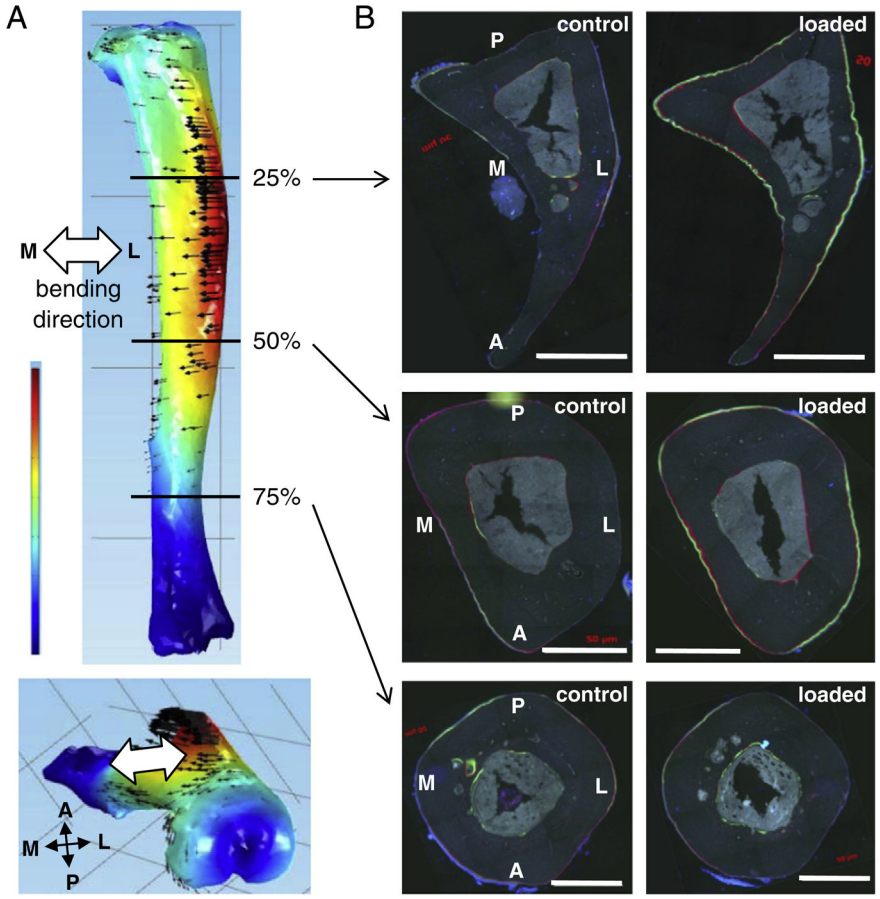

Fig. 7.

Tibia loading for bending analysis and histology. (A) Tibia bending direction, predicted by a FE analysis. The bending direction is mainly along the mediolateral direction (M–L), and the major displacement takes place between 25% and 50% along the length of the tibia from the proximal end. The color code indicates a magnitude of displacement (red—highest displacement; and blue—lowest displacement), and the black arrows suggest the bending directions. (B) Fluorescently double-labeled tibia cross-sections at the proximal (25%), middle (50%), and distal (75%) positions. The left images are controls, and the right images tibia loading. The letter labels are: P—posterior; A—anterior; M—medial; and L—lateral. Bar=500 μm.